ARTICLE

Large-Area Surface-Enhanced Raman Spectroscopy Imaging of Brain Ischemia by Gold Nanoparticles Grown on Random Nanoarrays of Transparent Boehmite

Shogo Yamazoe,[†,‡] Masayuki Naya,[†,*] Megumi Shiota,[†,‡] Takayuki Morikawa,[‡,§] Akiko Kubo,[‡,§] Takeharu Tani,[†] Takako Hishiki,[‡,§] Tadashi Horiuchi,[‡,§] Makoto Suematsu,[‡,§] and Mayumi Kajimura[‡,§,*]

[†]Frontier Core-Technology Laboratories, R & D Management Headquarters, FUJIFILM Corporation, 577, Ushijima, Kaisei-machi, Ashigarakami-gun, Kanagawa 258-8577, Japan, [‡]Department of Biochemistry, Keio University School of Medicine, Tokyo 160-8582, Japan, and [§]JST, ERATO, Suematsu Gas Biology Project, Tokyo 160-8582, Japan

ABSTRACT Although SERS spectroscopy, which is sensitive to molecular vibration states, offers label-free visualization of molecules, identification of molecules and their reliable large-area imaging remains to be developed. Limitation comes from difficulties in fabricating a SERS-active substrate with homogeneity over a large area. Here, we overcome this hurdle by utilizing a self-assembled nanostructure of boehmite that is easily achieved by a hydrothermal preparation of aluminum as a template for subsequent gold (Au) deposition. This approach brought about random arrays of Au-nanostructures with a diameter of ~125 nm and a spacing of <10 nm, ideal for the *hot-spots* formation. The substrate, which we named "*gold nanocoral*" (GNC) after its coral reef-like shape, exhibited a small variability of signal intensities (coefficient value <11.2%) in detecting rhodamine 6G molecule when 121 spots were measured over an area of 10 × 10 mm^2, confirming high uniformity. The transparent nature of boehmite enabled us to conduct the measurement from the *back-side* of the substrate as efficiently as that from the *front-side*. We then conducted tissue imaging using the mouse ischemic brain adhered on the GNC substrate. Through nontargeted construction of two-dimensional-Raman-intensity map using differential bands from two metabolically distinct regions, that is, ischemic core and contralateral-control areas, we found that mapping using the adenine ring vibration band at 736 cm^{-1} clearly demarcated ischemic core where high-energy adenine phosphonucleotides were degraded as judged by imaging mass spectrometry. Such a detection capability makes the GNC-based SERS technology especially promising for revealing acute energy derangement of tissues.

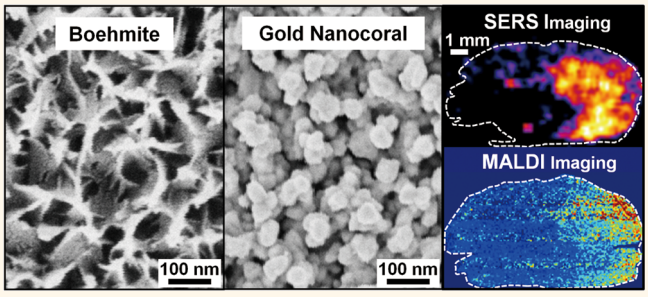

KEYWORDS: ischemia detection · template-guided self-assembly · biosensor · gold nanocoral · 3D-FDTD · *back-side* detection · emission pattern

Surface-enhanced Raman scattering (SERS) can provide information on the structure of molecules based on vibrational fingerprints[1,2] without labeling. High sensitivity of SERS to detect molecules in trace amounts has been applied to biomedical spectroscopy.[3] In particular, an indirect application of SERS using a reporter molecule attached to Au- or Ag-nanoparticles has been successful in imaging molecular dynamics within the cell[4] including sensing DNA hybridization,[5] the redox potential,[6] and localized pH of a single live cell.[7]

Unlike such small-area SERS imaging at the level of cells utilizing nanoparticles, large-area imaging to detect native biomolecules at the level of tissues has been limited. The reason behind this comes from the difficulty to construct a SERS-active substrate which ensures formation of '*hot spots*', localized regions of intense local field enhancement,[8] providing strong enhancement of Raman signals uniformly over a large-surface area. Recent advance to overcome such a hurdle includes various lithographic processes that enable precise control of ordering and periodicity of metal nanostructure constituting an ideal geometry for the SERS ability.[9,10] However, elaborate and time-consuming procedures make

* Address correspondence to masayuki.naya@fujifilm.com, myk30@z5.keio.jp.

Received for review December 23, 2013 and accepted May 27, 2014.

Published online May 27, 2014
10.1021/nn4065692

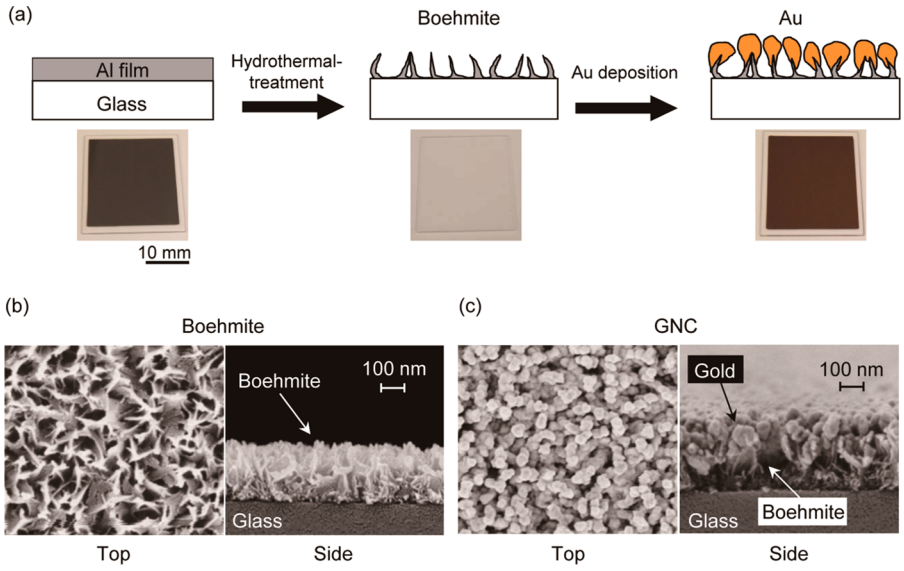

Figure 1. Process to fabricate the gold nanocoral (GNC) substrate. (a) The GNC is produced using the following three steps: (i) depositing aluminum (Al) into a film layer; (ii) immersing the Al film into boiling water to form thin, sharp-edged leaf-like superstructure of boehmite; and (iii) depositing Au on the boehmite template. Photograph of the 24 × 24 mm^2-substrate at each stage is shown. Note that hydrothermal treatment converts an opaque Al film to a transparent boehmite. SEM images showing top and side views of boehmite, random arrays of leaf-like structures (b) and GNC, a coral reef-like structure (c).

them far from practical. Instead of using the lithographic process, one simple approach is to utilize a self-assembled structure as a template.[11−13] In this study, we materialized hydrothermal preparation of boehmite (aluminum oxide hydroxide, AlO(OH)) which produces a self-assembled nanostructure with boiling a layer of aluminum.[14] This simple process brings about random arrays of nanostructure of boehmite serving as a robust template for the Au deposition ensuring strong enhancement of Raman signals.[11−13,15−17] Here, we report this simple, reproducible, and cost-effective method to fabricate a novel SERS substrate covering 24 × 24 mm^2, large enough for the tissue imaging.

From a viewpoint of life sciences, we need a comprehensive strategy to characterize metabolic profiles in distinct regions of tissues, *e.g.*, tumor *versus* nontumor regions, or ischemic *versus* normal regions. Powerful capability of matrix-assisted laser desorption ionization (MALDI)/imaging mass spectrometry (IMS)[18−20] and magnetic resonance spectroscopy (MRS)[21,22] to identify compounds has been intensively utilized for such imaging analyses. However, instruments for MALDI-IMS and MRS can be prohibitively expensive for many laboratories. We, thus, aimed to apply the newly engineered SERS substrate, named '*gold nanocoral*' (GNC), as an alternative technology to detect regional metabolic derangement. We examined if the GNC is capable of demarcating ischemic regions of the mouse brain defining an area of 10.4 × 8 mm^2, which covers much wider area than any of previously conducted SERS imaging.[7] The results demonstrated that GNC can sense ischemia by clearly demarcating metabolic derangement of 9-substituted adenine derivatives at an acute phase of ischemia.

RESULTS AND DISCUSSION

Fabrication of Gold Nanocoral (GNC) Substrate Using Transparent Boehmite As a Template. The GNC substrate was prepared in three steps (Figure 1a). First, we deposited a thin layer of aluminum (~20 nm in thickness) on the glass (24 × 24 mm^2). Second, we boiled the film in hot water. This hydrothermal procedure transformed the flat-aluminum film into random arrays of leaf-like nanostructures with a height of ~200 nm at an interval of ~125 nm (Figure 1b, see also Figure S1). Third, Au was deposited on the surface of the boehmite-template (Figure 1c). This procedure initiated the growth of Au spheres on the ledge, but not on the valley, of the boehmite structure; such a phenomenon can be explained by the island, or Volmer−Weber growth mechanism (see Figure S1 for details).[23,24] We named resultant substrate '*gold nanocoral*' (GNC), because this structure resembles a coral reef. The three-step procedure which is simple and rapid enabled us to fabricate the GNC substrate with good reproducibility.

Optimizing SERS Enhancement by Controlling Amount of Au Deposition. To optimize SERS signal enhancement, the size of Au particles that coat the boehmite surface was systematically modified by varying the amount of Au deposition on the boehmite. Figure 2a shows SERS signal intensity from rhodamine 6G (R6G) as a function of the thickness of Au (d_{Au}) on a plain glass. The d_{Au} was used as a practical indicator for Au deposition because it was not feasible to measure the actual Au thickness on the boehmite during the deposition process. SERS signal intensities increased progressively as the d_{Au} increased from 30 to 90 nm, but started to decline with further thickening in d_{Au}. On the basis of this result, we determined 90 nm as an optimal d_{Au} for SERS.

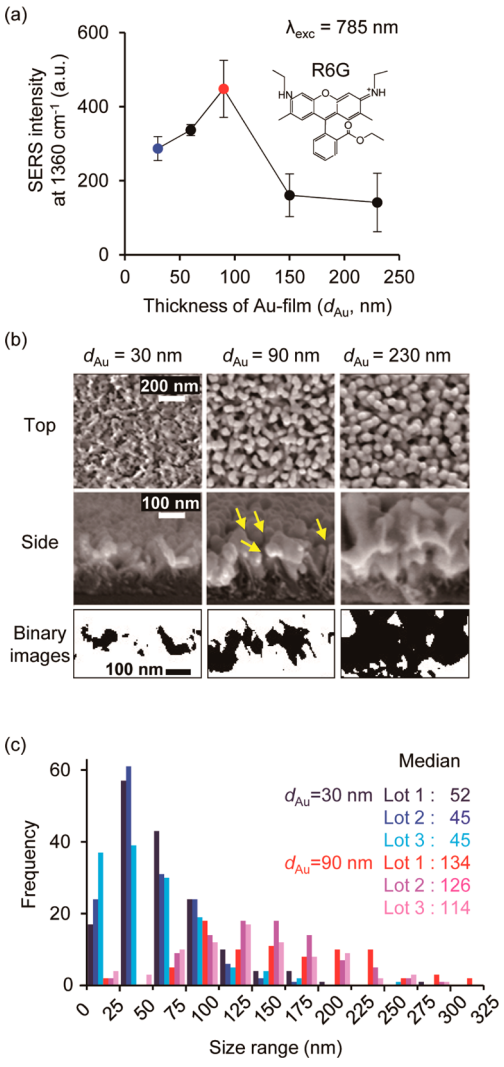

Figure 2. SERS sensitivities of GNC substrates controlled by amounts of Au deposition. (a) SERS signal intensities of GNC substrate to rhodamine 6G (R6G) at 1360 cm^{-1} are plotted against the thicknesses of Au (d_{Au}, used as an indicator for the amount of Au deposition on the boehmite, see text). In this experiment, an aliquot of 40 μL of an R6G solution (100 μM) was deposited on the GNC and dried in air. A 785 nm laser with 0.5 mW power was focused on the sample by a ×20 objective lens (NA 0.4), with the acquisition time of 10 s. Note that 90 nm in d_{Au} (the red symbol) achieved the highest signal. (b) SEM images showing top and side views of the GNC with varied d_{Au}. Note that, with 30 nm of d_{Au}, particles are not aggregated; with 230 nm of d_{Au}, particles tend to overgrow leaving no gap between them; with 90 nm of d_{Au}, particles form random arrays with <10 nm-gaps among them (arrows). Bottom panel: binary images of side views of the GNC to highlight gold. (c) Frequency histograms of Au-particle sizes observed under 30 and 90 nm d_{Au}. Histograms were constructed based on 447 and 252 particles measured under 30 nm- (bluish) and 90 nm- (reddish) d_{Au}, respectively.

Images of the GNC with different d_{Au} obtained using scanning electron microscopy suggest an explanation for these results. As the d_{Au} thickened, the size of Au nanoparticles increased gradually; consequently, gaps between adjacent particles decreased progressively (Figure 2b). When d_{Au} was 230 nm, neighboring Au particles fused together, causing diminished interparticle gaps. In contrast, when d_{Au} was 90 nm, random arrays of Au nanostructures with a particle diameter of ~125 nm and a spacing of <10 nm were formed. This Au diameter and spacing are ideal for the *hot-spots* formation, and thus provided us with optimum SERS signal intensity.

The GNCs created using our technique are reproducible. Figure 2c shows lot-to-lot variations of Au particle-sizes from three independent production lots. As expected, the median (±interquartile range) values for particle sizes depended on the d_{Au} (48 (±30) and 125 (±93) nm for 30 and 90 nm of d_{Au}, respectively, n = 3 for each d_{Au}). Unlike lithographically patterned substrates which produce no variations, the GNC production method that we employed produces some variation as evident in these histograms (Figure 2c). However, average values obtained from three different production-lots were within a narrow range (range of 7 and 20 nm for d_{Au} of 30 and 90 nm, respectively) indicating high reproducibility of this procedure.

Experimental Estimation of Analytical Enhancement Factors (aEF). To quantify the overall enhancing magnitude of signal intensities provided by the GNC substrate, we empirically determined the analytical enhancement factors (aEF) (see Methods for details). Here, the Raman signal obtained in the presence of the GNC, and those obtained under the nonenhanced condition, was used to calculate an aEF value. The signal obtained using the boehmite substrate without Au was used as a nonenhanced signal.

Table 1 shows results for the aEFs using R6G as a target analyte (see also Figure S2 for typical spectra showing the Raman bands). The aEF of the GNC substrate was found to be 1.4 × 10^4 at 1359 cm^{-1}. This value was 2 orders of magnitude lower than the aEF value (~10^6) obtained from an Au-based substrate in the form of immobilized nanorod assemblies (INRA) with particle size of 600 nm (5 times larger than ours), adjusted for optimal signal excitation at 785 nm.[25] With our GNC manufacturing procedure, the maximum Au-sphere size is limited by the periodicity of the boehmite nanostructure to ~125 nm (see Figure 1S). One possible solution to overcome such a constraint is depositing Au at an oblique angle rather than a perpendicular angle, which is known to improve SERS activities.[26,27]

In addition, we have compared the aEF obtained from the GNC substrate with that obtained using the

TABLE 1. Raman Active Mode of R6G with SERS and Non-SERS Frequencies and Corresponding aEFs

ν_i (SERS) [cm^{-1}]	ν_i (Raman) [cm^{-1}]	aEF
611	611	2.5 (±1.0) × 10^4
1196	1183	3.0 (±1.0) × 10^4
1359	1361	1.4 (±0.6) × 10^4
1508	1510	1.0 (±0.4) × 10^4

commercially available, lithographically patterned substrate[28] under the same experimental conditions. As seen in Figure S3, our GNC substrate achieved similar (although slightly smaller) enhancing magnitude to this solid state substrate. Together with the uniformity discussed later (Figure 5), estimated values of aEF ensure the GNC as a useful SERS-active substrate.

SERS Activities Obtained from *Front-Side* and *Back-Side* of the GNC Substrate. One potential source of error in conducting tissue imaging with SERS could arise from distortions of absorption, scattering and/or refraction characteristics due to inhomogeneity of the refractive indices within the tissue.[29] If we can direct the exciting light from the back side of the substrate without penetrating such inhomogeneous tissues and collect the scattered radiation, such a configuration (*back-side*) can minimize a problem. Here, we thought of taking advantage of the transparent nature of boehmite. We thus compared SERS intensities of 1360 cm^{-1} band of dry-state rhodamine 6G (R6G) obtained by both the *front-side* and the *back-side* configurations. As shown in Figure 3, signal intensity from the *back-side* configuration was ~0.7-fold of that with the *front-side* configuration. Given that neither can the laser beam at 785 nm penetrates the Au layer (only 2% transmission and 63% extinction, Figure S4) nor the Raman radiation can transmit through the layer, the observation that the *back-side* configuration achieves comparable Raman signals as with the *front-side* configuration is not intuitive. We, therefore, examined the mechanisms behind this phenomenon by the three-dimensional-finite difference time-domain (FDTD) simulation below.

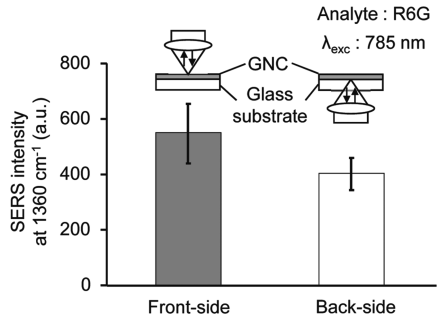

Figure 3. SERS signal intensity of R6G at 1360 cm^{-1} measured from the *front-side* and *back-side* of the GNC substrate. SERS signal intensity of R6G at 1360 cm^{-1} measured from the *front-side* and the *back-side* of GNC substrate are compared. Note that these signals are comparable. A 785 nm laser with 0.8 mW power was focused on the sample by a ×20 objective lens (NA 0.4), with the acquisition time of 10 s.

Deciphering SERS Enhancement Mechanisms by Three-Dimensional-FDTD Simulation. Figure 4a represents the geometry of our SERS device. For the simulation, we simplified the geometric model to a single dimer of Au nanospheres in air.

Although previous investigators have simulated the SERS enhancement, the calculation was based on the standard E^4 approach.[30] In such an approach, the SERS enhancements were assumed to be proportional to the second power of G_{loc} (local field enhancement), the first term in eq 2 in Methods. Here, we attempted more rigorous simulation in which G_{rad} (radiation enhancement), the second term in eq 2, is included into the calculation since the radiation pattern of electric field (E-field) intensity distributions is central to our argument.

Figure 4b shows the localized E-field intensity distributions when a dimer is irradiated by the *x*-polarized

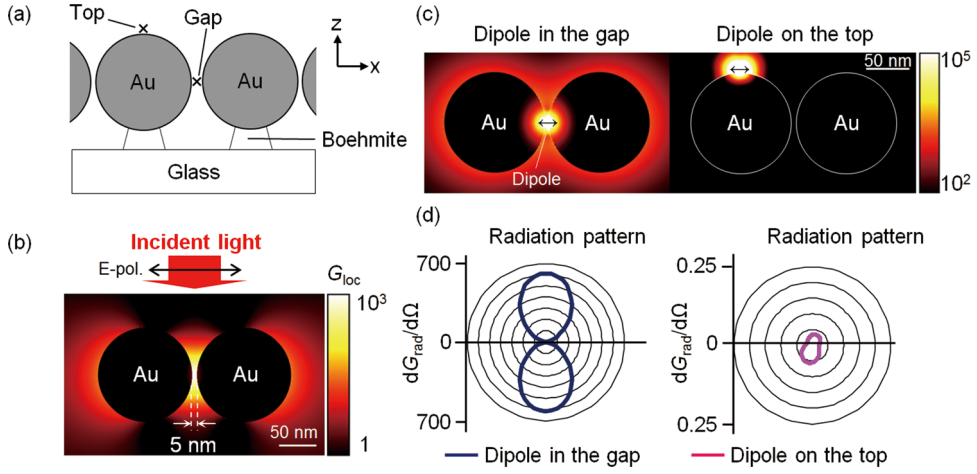

Figure 4. FDTD simulations of the SERS enhancement factor. (a) Side-view illustration of the GNC substrate geometry. (b) Calculated E-field intensity distributions for an Au dimer excited by *x*-polarized plane-wave light at 785 nm. In the simulation, we simplified the model geometry to a dimer formed by two Au spherical particles with a 100 nm diameter separated by a 5 nm gap. Unlike the large local field enhancement in the gap of the dimer, no enhancement occurs on the top of the dimer. (c) Calculated E-field intensity distributions of an Au dimer when an oscillating dipole is located in the gap (left) or on the top (right) of the dimer. E-field intensity is normalized with respect to the total power radiated from a dipole in free-space. Note that the dimer excited with a dipole in the gap gives off a large power; conversely, the one excited with a dipole on the top results in overall quenching. (d) Angular dependency of the radiation intensity ($dG_{rad}/d\Omega$: power radiated in the far-field per unit angle in a given direction) produced by each oscillating dipole. Note that little energy is radiated in the far-field from the dipole on the top compared to that in the gap of the dimer.

plane-wave light (λ = 785 nm) from the *front-side*. A striking enhancement of the E-field intensity (G_{loc_gap} = 930) in the gap takes place, whereas no enhancement (G_{loc_top} = 1.1) occurs on the top. Importantly, the E-field intensity pattern is symmetrical with respect to the interparticle axis of the dimer. Thus, either the incident light comes from the *front-side* or the *back-side* does not make any difference in the localized E-field intensity distributions, supporting our observation seen in Figure 3.

Figure 4c shows the radiated E-field intensity distributions when an oscillating dipole is located at either in the gap or on the top. Instead of using 785 nm, wavelength of the incident light, we calculated the E-field intensity using a Raman Stokes wavelength of 880 nm corresponding to a 1360 cm^{-1} band of R6G. The E-field intensity originated from the dipole in the gap is remarkably enhanced. When the orientation of dipole-oscillation is perpendicular to the Au surface, the dipole-oscillation is coupled to radiative localized plasmon resonances of the dimer which in turn causes the dipole to radiate more energy (G_{rad_gap} = 610).[31,32] Conversely, when a dipole is located on the top, no enhancement but quenching of the radiated power (G_{rad_top} = 0.04) takes place. Because the orientation of the dipole-oscillation is parallel to the Au surface, the dipole cannot couple to radiative localized plasmon resonances which causes quenching rather than enhancement of radiation.[31,32] To our knowledge, our simulation is the first pictorial view of E-field intensity distributions of a dimer originated from a Raman dipole. One important feature of our simulation is the contour presentation for the power radiated in the far-field per unit angle in a given direction ($dG_{rad}/d\Omega$) produced by each oscillating dipole (Figure 4d). The dipole in the gap radiates more power to the axis perpendicular to the interparticle axis of a dimer, which is isotropic to both *front-* and *back-sides*. It is this radiation that we detect in the far-field as a signal. Conversely, little energy is radiated in the far-field from the dipole on the top.

The simulation supports our observation that the *back-side* configuration achieved comparable Raman signals as the *front-side* configuration (Figure 3). Such an observation can be explained by two reasons. One is that the Raman signal from molecule on the top is negligibly small ($G_{R\_top} \sim 0.04$), while that from the gap is exceedingly large ($G_{R\_gap} \sim 5.7 \times 10^5$) as indicated in Table 2. The other is that the dipole radiation from molecule in the gap is isotropic to both *front-* and *back-sides* (Figure 4d).

TABLE 2. Enhancement Factors (EF) of Local Field, Radiation, and Raman on the Top and in the Gap

	EF_{top}	EF_{gap}
G_{loc}	1.1	930
G_{rad}	0.04	610
G_R	~0.04	~5.7×10^5

Uniform SERS Sensitivity Exhibited by the GNC. To examine if the GNC substrate ensures uniform SERS sensitivity, we measured the SERS signals of R6G. In this experiment, the GNC substrate was immersed into an R6G solution (10 μM) for 15 min, rinsed lightly by pure water, and dried in air. We recorded SERS spectra from 121 points covering an area of 10 × 10 mm^2 with a 1 mm-translation step. Figure 5a displays spot-to-spot mapping of SERS intensities for the 1360 cm^{-1} band characteristic to the aromatic C−C stretching vibrations of R6G.[33] The coefficient of variation from these 121 data was within 11.2 ± 0.2% (n = 3), confirming high uniformity. Figure 5b shows SERS spectra taken from 11 points from the sixth row of the matrix shown in Figure 5a. Here, the background was subtracted. Autocorrelation coefficients of these spectra are more than 0.993. The result indicates that the GNC has high uniformity of the SERS signal over the large area compared

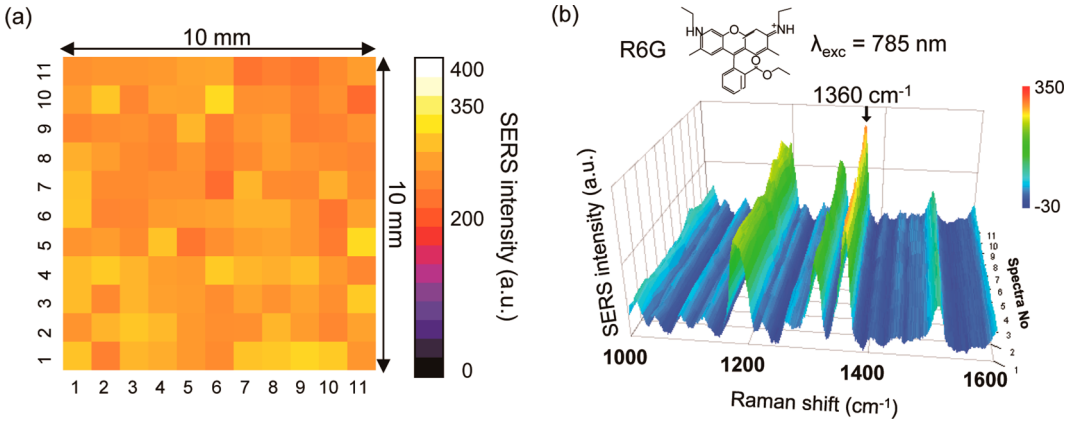

Figure 5. High uniformity of SERS sensitivity over a large-area GNC. (a) Spot-to-spot mapping of SERS intensities at 1360 cm^{-1} band characteristic to R6G. SERS intensities measured at 11 × 11 pixels show a small variation. (b) The SERS spectra taken from 11 spots from the 6th row of the matrix in panel a. These spectra are almost identical. For this experiment, we used a ×20 objective lens (NA 0.4) with a laser power of 1.7 mW and acquisition time of 5 s.

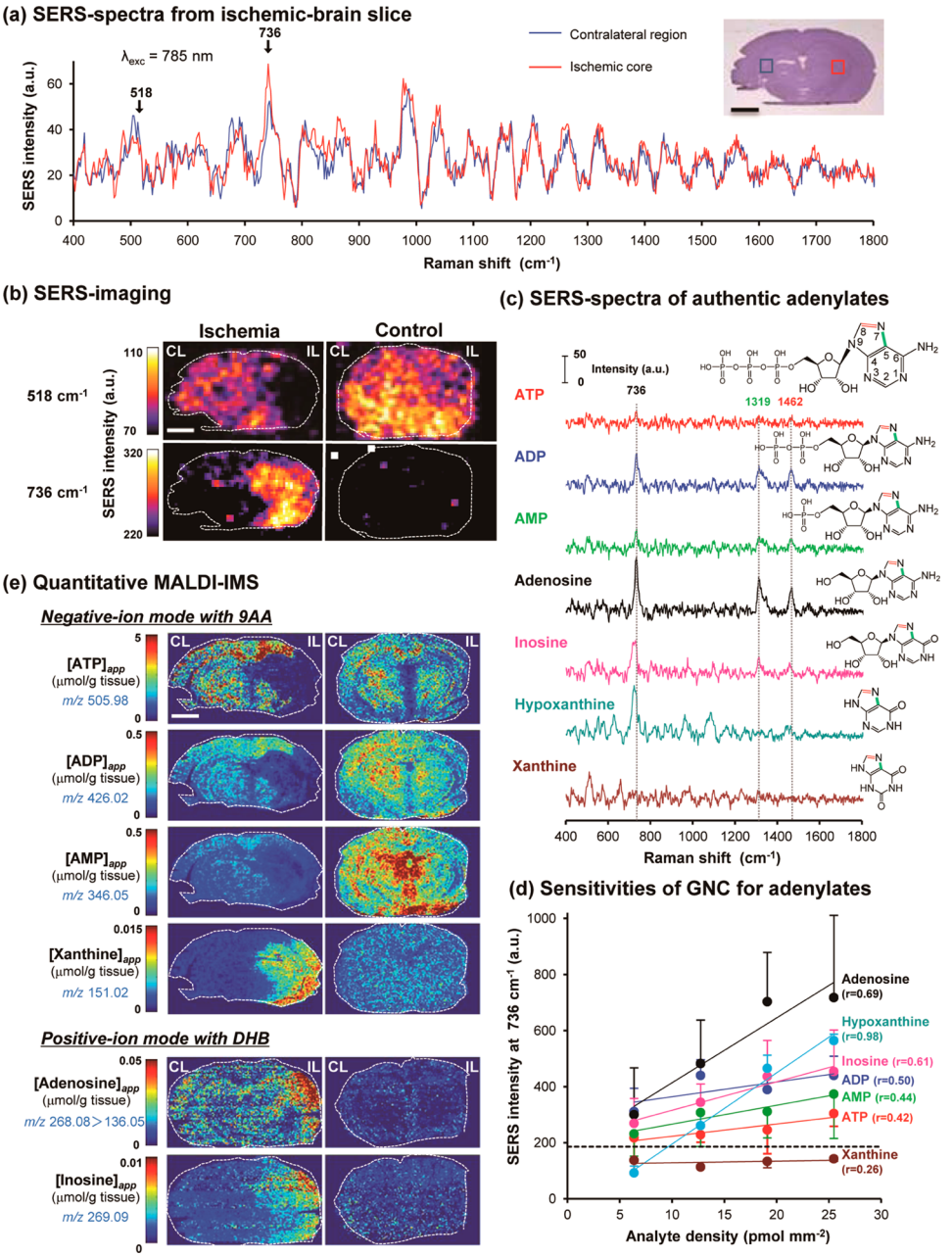

Figure 6. Large-area SERS imaging of ischemic brain. (a) SERS spectra from two specific regions of the ischemic brain. These spectra are the average of 5 data points in an area of 1 × 1 mm^2 from ischemic core (red) and its contralateral region (blue). A 785 nm laser with 1.7 mW power was focused on the sample by a ×60 objective lens (NA 0.7), with the acquisition time of 2 s. (b) The relative intensity of the Raman bands with 518 ± 5 and 736 ± 15 cm^{-1} are used to map the ischemic region of the mouse brain. Images are representative of 3−4 independent experiments. Note the complementary patterns of images of 518 and 736 cm^{-1}; *i.e.*, the signals at 518 cm^{-1} from the ischemic core is smaller than that from the contralateral hemisphere, whereas the pattern is reversed at 736 cm^{-1}. (c) SERS-spectra of authentic adenylates with area density of 19.2 pmol mm^{-2}. Note the strong Raman peaks at 736, 1319, and 1462 cm^{-1}, which reflect adenine-ring breathing, the C5−N7- (green), and the N7−C8- stretch (red) modes, respectively. (d) Relative sensitivity of the GNC substrates to adenine related compounds. SERS signal intensities are plotted as a function of surface densities of each analyte. Data are collected from three independent preparations (see Figure S6 for individual data). Note that the GNC displays higher sensitivities to adenosine, hypoxanthine, and inosine than to ATP, ADP, AMP, and xanthine. Dashed line indicates the noise level of measurement. A 785 nm laser with 1.7 mW power was focused on the sample by a ×60 objective lens (NA 0.7), with the acquisition time of 2 s. (e) Quantitative imaging mass spectrometry (Q-IMS) showing spatial distribution of apparent tissue contents of various adenylates. Q-IMS analysis was conducted using a semiserial section with 10-μm thickness prepared from the same animal with which the SERS imaging was conducted as in (b). Focal ischemia was induced by a left middle cerebral artery occlusion. Control group underwent a 60 min period without an occlusion. Content maps for ATP, ADP, AMP, and xanthine and those for adenosine and inosine are constructed on a same tissue with negative-ion and positive-ion mode, respectively. In the ischemic core, $[ATP]_{app}$, $[ADP]_{app}$, and $[AMP]_{app}$ are substantially decreased, whereas $[adenosine]_{app}$, $[inosine]_{app}$, and $[xanthine]_{app}$ are elevated due to purine degradation induced by ischemia. Note that the ischemic core exhibits a marked increase in xanthine, adenosine, and inosine matching with the area depicted by the SERS-imaging in panel b. Images are representative of 3−4 independent experiments. Scale bars = 2 mm.

with other SERS two-dimensional-substrates.[25,28,34−36] Here, it should be noted that, unlike the nanostructure created by a lithographic process, geometric structure of boehmite is not periodic (Figure 1b). On the contrary, sizes of Au particle and interparticle gap are inhomogeneous (Figure 1c). However, given that the spot-size of the excitation beam (~6 μm) is one-order larger than the size of the Au particle (~125 nm), the spatial averaging of *hot-spots* on a macroscopic scale makes the GNC an efficient SERS substrate capable of providing uniform SERS sensitivity over the large-surface area.

SERS Imaging at 736 cm^{-1} Reveals Brain Ischemia. Our goal was to determine if the GNC substrate could be used to detect metabolic alterations that occur as disease (such as ischemia) progresses. As a first step, we conducted large-area imaging of ischemic brains. Ischemia was induced by unilateral middle cerebral artery (MCA) occlusion such that tissue metabolism was severely compromised on the side of the brain ipsilateral to the occlusion, while the contralateral side was less affected. Thus, the MCA model allowed us to determine if the GNC substrate can detect the metabolic differences between the two sides of the brain, with each half having a surface area over 5.2 × 8 mm^2.

Figure 6a shows SERS spectra from two specific regions of an ischemic brain adhered on the GNC substrate: *i.e.*, (i) an ischemic core from the hemisphere ipsilateral to the occlusion (red) and (ii) a region contralateral to the ischemic core (blue). The SERS signal around 500 cm^{-1} from the ischemic core is smaller than that from the contralateral region. Conversely, the opposite is the case for the signal around 736 cm^{-1}. SERS images using both 518 and 736 cm^{-1} revealed the core region of ischemia (Figure 6b). With 518 ± 5 cm^{-1}, the core is depicted as a low-signal area. By contrast, with 736 ± 15 cm^{-1}, the core appears as a high-signal area. Thus, these patterns complement each other forming a metabolically delineated boundary at the interface between the ischemic core and the nonischemic region. Although the molecular species causing the 518 cm^{-1} shift is yet to be determined, the knowledge that a strong Raman band around 736 cm^{-1} arises from vibrations of the adenine ring[37] led us to examine if 9-substituted adenine derivatives are the origin of the enhanced signals. Indeed, ischemia causes massive degradation of ATP which results in increases in purine degraded metabolites suggested by the CE-MS analysis as described previously in our study.[18] (Figure S5).

Thus, we next examined sensitivities of the GNC substrate to ATP, ADP, AMP, adenosine, inosine, hypoxanthine, and xanthine. Figure 6c shows the typical SERS spectra for these species of molecules. ATP, ADP, AMP, and adenosine exhibit three bands at 736, 1319, and 1462 cm^{-1}, which most likely arise from adenine-ring breathing, the C5-, N7-, and the N7−C8- stretch modes, respectively.[37] With inosine and hypoxanthine for which a primary amine attached to C-6 of adenine is replaced by an oxygen atom, the band around 736 cm^{-1} is slightly shifted to the left. With xanthine, the band at 736 cm^{-1} is completely absent, ruling out its possibility as a candidate molecule that delineates the ischemic core in SERS imaging. Figure 6d shows plots of graded densities (6.4−25.5 pmol mm^{-2}) of analytes against SERS intensities at 736 cm^{-1}. Correlation coefficients are considerably greater for adenosine, hypoxanthine and inosine than for ATP, ADP, and AMP (see also Figure S6). The result raises a possibility that the GNC is more sensitive to adenosine, hypoxanthine, and inosine than to ATP, ADP, and AMP under the current experimental conditions. This argument can be further supported by the results of quantitative IMS (Q-IMS) and CE-MS (Figure S5). In the control brain, Q-IMS indicates large amounts of ATP, ADP and AMP (Figure 6e), whereas by SERS, these metabolites are not detected as high signals at 736 cm^{-1} (Figure 6b). In the ischemic brain, on the other hand, the increased adenosine and inosine in the ischemic core displayed by Q-IMS (Figure 6e) matches to the SERS imaging with 736 cm^{-1} (Figure 6b). These results suggest that increases in adenosine, inosine and hypoxanthine are responsible for an increase in ischemia-induced SERS signals.

Finally, it is important to emphasize that there has been limited methods available to detect local metabolic alteration at acute phases of ischemia (<60 min), particularly for small animals. Indeed, functional staining with 2,3,5-triphenyltetrazolium chloride (TTC), a conventional method to delineate the infarction,[38] cannot be used to detect biochemical alterations at 60 min postischemia (Figure S7). Similarly, cresyl violet and hematoxylin and eosin stainings, often used in small animal studies, can detect histological abnormality only at much later time-points, typically at least 48 h after ischemia. Therefore, our data that demonstrate the detection capability of GNC-based SERS delineating the ischemic core at an onset of ischemia makes it especially promising for revealing acute biochemical alterations occurring before irreversible damages *in vitro* and *in vivo*.

CONCLUSIONS

We have designed a novel SERS-active substrate, named '*gold nanocoral*' (GNC) capable of enhancing SERS signals with high uniformity over the large area with ease. Such technical breakthrough was achieved by utilizing a self-assembled nanostructure of boehmite as a template for the subsequent Au-deposition. The use of boehmite can offer 2-fold benefits. First, a simple and rapid hydrothermal process of aluminum film that produces sharp geometry of boehmite makes it easy to produce a large-area SERS substrate. It could revolutionize the elaborate and time-consuming procedures such as lithography. Second, the transparent

nature of boehmite enabled the SERS measurement from the *back-side* of the GNC.

The *back-side* mode can be advantageous over the *front-side* mode especially when dealing with tissues. Since tissues consist of different types of cells, *e.g.*, eye ball consisting of transparent lens and opaque retina, the local index of refraction can vary greatly within one tissue. With the *front-side* mode, both exciting and emitting lights must travel through an inhomogeneous medium; thus, such configuration may cause distortion in the magnitude of SERS signals, but with the *back-side* mode, such a potential problem can be avoided. Furthermore, since the incoming wavefront excites the GNC without penetrating the samples, such unique characteristics can be exploited by chemical analyses of the surface on any opaque substrates. A wide range of application includes clinical diagnosis of dehydrated blood, biochemical examination of any thick-tissue samples, and industrial use for surface chemical analysis.

We have demonstrated the large-area SERS imaging where GNC substrate made it possible to visualize the ischemic core of mouse brain without labeling and pretreatment of the tissue. Although our imaging is the first to apply SERS to demarcate metabolic derangement occurring at the ischemic region, we are unable to definitively assign the molecules responsible for the change. This is because chemical identification by SERS is based on the vibrational fingerprint arising from unique chemical structures, not from the whole molecule. SERS technology, therefore, requires further efforts to ensure quantification and identification of molecular species. Unlike the MALDI/IMS that relies on the ionization of the analytes, SERS has strength in visualizing multiple metabolites as they exist in the tissue without any chemical pretreatment. Such characteristics should be exploited further. It should be noted that some metabolites, *e.g.*, glucose and urea, are difficult to ionize; thus, MALDI cannot detect molecules of this kind. We believe that a large-area SERS devise will give rise to new insights to characterize complex metabolic interactions between distinct regions of tissues such as tumor *versus* nontumor regions and ischemic *versus* normal regions. Such strategy will provide means for elucidating molecular mechanisms for disease progress and fulfill control functions.

METHODS

Fabrication of the Gold Nanocoral. A 24 × 24 × 0.5 mm^3 glass plate was washed with acetone and methanol in an ultrasonic bath to remove organic contaminants. Aluminum (Al) was deposited on the plate at a 20 nm thickness with a reactive DC magnetron sputtering system (SPF-530H, ANELVA) at a deposition rate of 5 Å s^{-1}. Subsequently, the Al film was boiled in hot water (100 °C) for 5 min to form boehmite (AlO(OH)), and was dried with N_2 gas. Finally, Au was deposited on the boehmite nanostructures by electron−beam evaporation system (EBX-8C, ULVAC). We discovered that this process must be carefully controlled for Au particles to grow to optimal sizes such that SERS signal can be maximally enhanced. However, there was no practical way to measure the size of the Au particle on the boehmite during the fabrication process. We, thus, measured thicknesses of Au (d_{Au}) deposited on plain glass surfaces without boehmite layers, because a given deposition protocol generated d_{Au} well correlated with the Au-particle size. To estimate d_{Au}, a film-thickness gauge based on a crystal oscillator in the deposition system was used. All processes were conducted in a cleanroom. As described in the text, Au tended to accumulate and to grow on the ledge, but not at the valley, of boehmite nanostructure (see Figure S1 for details).

Morphological Analysis. To determine periodicity of the boehmite nanostructure (Figure S1), binary maps were created from top-view SEM images. Ledge-to-ledge distances were measured by connecting the center of ledge-like structures manually using ImageJ.

To examine the size variation of Au spheres, binary maps were created from side-view SEM images. After removal of particles whose diameters were <5 nm, sizes of the remaining particles were measured using the "analyze particles" function of ImageJ (Figure 2). To evaluate lot-to-lot reproducibility, frequency histograms of the particle size were constructed using three different production-lots from each of two d_{Au} groups, the 30 and the 90 nm.

SERS Measurements. To measure SERS signals in relation to d_{Au}, we used Raman microscope (Horiba, LabRam HR800) equipped with a ×20 objective lens (NA 0.4) and a 785 nm-diode laser. For the rest of experiments, we used a custom-made inverted microscope system (Figure S8) equipped with a fiber-coupled spectrograph (Ocean optics, QE65000), an *xy*-scanning stage with highest resolution of 250 nm, and a 785 nm-diode laser. Both microscope systems were calibrated by the 520 cm^{-1} silicon phonon mode before SERS measurements. The background noise was subtracted from the recorded spectra by the weighted mean fitting with Lanczos second function.

Experimental Estimation of Analytical Enhancement Factors (aEF). To estimate the analytical enhancement factors (aEF) of the GNC substrate, we used the method of Le Ru *et al.*[39] with some modifications. We used a higher laser power, a longer acquisition time, and more dense surface coverage of the probe molecules for the nonenhancing substrate than for the SERS-active GNC substrate (Figure S2). These modifications allowed us to obtain comparable and reliable signal intensities (see Figure S2) from both the SERS and nonenhancing Raman conditions. Thus, aEF in this study was defined as

$$\mathrm{aEF} = \frac{I_{SERS}/(P_{SERS} \times T_{SERS} \times N_{SERS})}{I_{RS}/(P_{RS} \times T_{RS} \times N_{RS})} \quad (1)$$

where I_{SERS} is the measured intensity from SERS-active substrate, while I_{RS} is that from nonenhancing substrate. P_{SERS} and P_{RS} are the power of excitation laser, T_{SERS} and T_{RS} are acquisition times, and $N_{SERS,}$ and N_{RS} are the number of probe molecule per unit effective area for adsorption for a SERS-active and normal Raman conditions, respectively.

Since this definition strongly depends on the properties of probe surface coverage, the care was taken to avoid multilayer formation of probe molecules in the SERS condition. Specifically, 80 μL of R6G solution (10 μM) was dispersed over the GNC substrate (24 × 24 mm^2) in the clean room. Assuming only the upper half surface of the particle is available for the R6G molecule to be adsorbed, such a three-dimensional structure increases the surface area by approximately twice compared to a flat, two-dimensional structure. Thus, the volume and concentration used in our experiments should result in coverage of one R6G molecule per ~2.4 nm^2. Considering that one R6G occupies an area of ~1.1 nm^2 (approximate hydrodynamic radius of this molecule; ~0.59 nm[40]), our condition appears to ensure a submonolayer condition which is a prerequisite for the

TABLE 3. Parameters Used in the Experimental Estimation for aEFs

	SERS	Raman
P (mW)	1.35	8.5
T (s)	10	300
N (pmol mm^{-2})	1.38	208
I (a.u.)		
611 cm^{-1}	374	426
1196 cm^{-1}	184	174
1360 cm^{-1}	180	373
1510 cm^{-1}	87	256

SERS measurement. We used the same optical parameters (the wavelength of 785 nm, the ×20 objective lens, spectrometer) to acquire SERS and Raman signals. All other parameters used in the experiment are tabulated above (Table 3). Lithographically patterned substrates (Klarite, KLA-313) were purchased from Renishaw (Tokyo, Japan).

Theoretical Calculations of the SERS Enhancement Factor Using FDTD. In terms of the electrical mechanism, the Raman enhancement (G_R) is expressed as the product of the *local field enhancement* (G_{loc}) and the *radiation enhancement* (G_{rad}):[31]

$$G_R \approx G_{loc} \times G_{rad} \quad (2)$$

G_{loc} is represented by the ratio of the *local field intensity* ($|\mathbf{E}_{loc}(\lambda)|^2$) against the *incident wave field intensity* ($|\mathbf{E}_{inc}(\lambda)|^2$) at the wavelength ($\lambda$) of the excitation:

$$G_{loc} = |\mathbf{E}_{loc}(\lambda)|^2 / |\mathbf{E}_{inc}(\lambda)|^2 \quad (3)$$

G_{rad} is represented by the ratio of the total radiated power from a Raman dipole located in the vicinity of an Au nanoparticle (P_{rad}) against that from a Raman dipole in free-space (P_{rad_free}):

$$G_{rad} = P_{rad} / P_{rad\text{-}free} \quad (4)$$

We used a custom-made three-dimensional FDTD software for the estimation of these enhancement factors and radiation patterns. The simulation models were the following: the diameter of the Au spheres was 100 nm. Two Au spheres were separated by a 5 nm gap. The dimer was placed in air with a refractive index of 1.0. In the case of the local field enhancement, the dimer was irradiated by the *x*-polarized plane-wave light at 785 nm. We calculated the localized field enhancement at the position on the top and in the gap of the dimer located at a 2.5 nm-distance from Au surface. The calculating volume was 285 × 180 × 180 nm^3. In the case of the radiation enhancement, the point source of dipole oscillating *x*-axis was located in the middle of the dimer gap and on the top of it with a 2.5 nm of distance from the Au surface. The calculating volumes in the case of top and gap were 245 × 140 × 160 and 245 × 140 × 140 nm^3. All these simulations were carried out with a grid size of 0.5 nm. The refractive indices of Au at 785 and 880 nm were 0.177 + 4.54*i* and 0.208 + 5.19*i*, respectively.[41]

Mouse Model of Cerebral Ischemia. Experiments were approved by the Animal Care and Utilization Committee of Keio University School of Medicine (approval number: 09046). Male C57BL/6J mice (22−26 g, Clea Japan, Tokyo) were anesthetized with isoflurane (4% for induction, 1.5−2% for maintenance) in 30% O_2/70% air. Rectal temperature was maintained at 36 ± 0.5 °C throughout. A focal brain ischemia was induced for 60 min by advancing a 6−0 nylon suture with its tip rounded to occlude the origin of a left middle cerebral artery as described previously.[18]

***In Situ* Freezing and Tissue Removal.** Brain is extremely susceptible to post-mortem changes in contents of cerebral labile metabolites such as adenylates. Thus, the best available methods must be employed to trap the metabolites as they exist *in vivo* and to minimize autolytic changes.[18,42] To achieve this, we employed the *in situ* freezing method which enables suspension of metabolic processes by rapidly lowering the tissue temperature while maintaining blood flow and oxygenation during the freezing process. To do so, mice were deeply anesthetized with diethyl ether and the head skin was trimmed. Tip of the head was dipped into liquid nitrogen with great care not to immerse the nose. Frozen brains were dissected with a surgical knife in a refrigerated box at −30 °C.

Large-Area SERS Imaging of Brain Tissues. Coronal sections with 10-μm thickness were cut with a cryomicrotome (CM1900, Leica Microsystems), and sections were thaw-mounted on the GNC substrate and kept in a vacuum chamber for 20 min. To construct two-dimensional-SERS map, spectra in the range of Raman shift between 300 and 2000 cm^{-1} were collected from 65 × 50 spots on a tissue covering the area of 10.4 × 8 mm^2 with a 0.16 mm-translation step. Acquisition time was 2 s for one spot. Integrated signals in ranges of 518 (±5) and 736 (±15) cm^{-1} are used for SERS images, which later were smoothed by averaging adjacent pixels using the ImageJ smoothing function. We used a × 60 (NA = 0.7) objective lens with optical correction rings. The incident beam was ∼2 μm in diameter and 33 μm in penetration depth with ∼1.7 mW power at a 785 nm laser.

Quantitative Imaging Mass Spectrometry (Q-IMS). Q-IMS was conducted as described previously.[18,43−46] Briefly, serial coronal sections with 10-μm thickness were cut with a cryomicrotome (CM1900, Leica Microsystems) and thaw-mounted on the indium tin oxide-coated glass slide (#578274, Sigma, Chiba, Japan) at −20 °C. For negative- and positive-mode analyses, 9-aminoacridine (9-AA, Kanto Chemical, 25 mM in 70% (v/v) methanol) and 2,5-dihydroxybenzoic acid (2,5-DHB, Bruker Daltonics 200 mM in 70% (v/v) methanol) were chosen, respectively. Each matrix was sprayed with airbrush (Procon boy FWA Platinum; Mr Hobby, Tokyo, Japan) on the specimens. The other frozen tissues were used for quantification of metabolites by CE/ESI/MS. MALDI mass spectra were acquired using MALDI-QIT-TOF mass spectrometer (Shimadzu Corporation, Kyoto, Japan).

Conflict of Interest: The authors declare no competing financial interest.

Acknowledgment. We are grateful to S. Hakuta for helpful suggestions for the early stage of our developing the three-dimensional-FDTD simulation. We thank A. Yamaguchi and M. Wachowiak for their invaluable editorial help. A preliminary report of our findings has been presented at the 58th Annual Meeting of The Japan Society of Applied Physics. Establishment of CE/ESI/MS was supported in part by Biobank Japan Project in MEXT, and Q-IMS was supported by a project in MAFF, Japan. This work was supported by Grant-in-Aid for Scientific Research 24500448 from the Japan Society for the Promotion of Science (to M.K.), and Japan Science and Technology Agency (JST), Exploratory Research for Advanced Technology (ERATO), Suematsu Gas Biology Project, in Tokyo, 160-8582 (to M.S.).

Supporting Information Available: Supporting Information is available on growth process of Au spheres on boehmite. This material is available free of charge *via* the Internet at http://pubs.acs.org.

REFERENCES AND NOTES

1. Kneipp, K. Surface-Enhanced Raman Scattering. *Phys. Today* **2007**, *11*, 40–46.
2. Moskovits, M. Surface-Enhanced Spectroscopy. *Rev. Mod. Phys.* **1985**, *57*, 783–826.
3. Wang, Y.; Yan, B.; Chen, L. SERS Tags: Novel Optical Nanoprobes for Bioanalysis. *Chem. Rev.* **2013**, *113*, 1391–1428.
4. Qu, L. L.; Li, D. W.; Qin, L. X.; Mu, J.; Fossey, J. S.; Long, Y. T. Selective and Sensitive Detection of Intracellular $O_2^{\bullet-}$ Using Au NPs/Cytochrome *c* as SERS Nanosensors. *Anal. Chem.* **2013**, *85*, 9549–9555.
5. Cao, Y. C.; Jin, R.; Mirkin, C. A. Nanoparticles with Raman Spectroscopic Fingerprints for DNA and RNA Detection. *Science* **2002**, *297*, 1536–1540.
6. Auchinvole, C. A.; Richardson, P.; McGuinnes, C.; Mallikarjun, V.; Donaldson, K.; McNab, H.; Campbell, C. J. Monitoring Intracellular Redox Potential Changes Using SERS Nanosensors. *ACS Nano* **2012**, *6*, 888–896.
7. Kneipp, J.; Kneipp, H.; Wittig, B.; Kneipp, K. One- and Two-Photon Excited Optical pH Probing for Cells Using Surface-

Enhanced Raman and Hyper-Raman Nanosensors. *Nano Lett.* **2007**, *7*, 2819–2823.
8. Maher, R. C. Surface-Enhanced Raman Spectroscopy: A Brief Perspective. In *Raman Spectroscopy for Nanomaterials Characterization*; Kumar, C. S. S. R., Ed. Springer: Heidelberg, 2012; pp 215−252.
9. Félidj, N.; Aubard, J.; Lévi, G.; Krenn, J. R.; Salerno, M.; Schider, G.; Lamprecht, B.; Leitner, A.; Aussenegg, F. R. Controlling the Optical Response of Regular Arrays of Gold Particles for Surface-Enhanced Raman Scattering. *Phys. Rev. B* **2002**, *65*, 0754191–0754199.
10. Yu, Q.; Guan, P.; Qin, D.; Golden, G.; Wallace, P. M. Inverted Size-Dependence of Surface-Enhanced Raman Scattering on Gold Nanohole and Nanodisk Arrays. *Nano Lett.* **2008**, *8*, 1923–1928.
11. Chan, S.; Kwon, S.; Koo, T. W.; Lee, L. P.; Berlin, A. A. Surface-Enhanced Raman Scattering of Small Molecules from Silver-Coated Silicon Nanopores. *Adv. Mater.* **2003**, *15*, 1595–1598.
12. Dick, L. A.; McFarland, A. D.; Haynes, C. L.; Van Duyne, R. P. Metal Film over Nanosphere (MFON) Electrodes for Surface-Enhanced Raman Spectroscopy (SERS): Improvements in Surface Nanostructure Stability and Suppression of Irreversible Loss. *J. Phys. Chem. B* **2002**, *106*, 853–860.
13. Naya, M.; Tani, T.; Tomaru, Y.; Li, J.; Murakami, N. Nanophotonics Bio-Sensor Using Gold Nanostructure. *Proc. SPIE* **2008**, *7032*, 70321Q.9.
14. Nakajima, A.; Fujishima, A.; Hashimoto, K.; Watanabe, T. Preparation of Transparent Superhydrophobic Boehmite and Silica Films by Sublimation of Aluminum Acetylacetonate. *Adv. Mater.* **1999**, *11*, 1365–1368.
15. Mourey, D. A.; Kasperchik, V.; Stasiak, J. W. SERS Structures with Nanoporous Materials. WO 2013130043 A1, Sep 6, 2013.
16. Patton, W. F.; Mikulskis, A.; Eva, G. Methods and Compositions for Detecting and Isolating Phosphorylated Molecules Using Hydrated Metal Oxides. WO 2006014424 A2, Feb 9, 2006.
17. Towata, A.; Lee, J.; Yasui, K.; Tuziuti, T.; Kozuka, T.; Iida, Y. Fabrication of Silver Nanoparticles Deposited on Boehmite Sol for Surface Enhanced Raman Scattering. *Appl. Surf. Sci.* **2011**, *257*, 6010–6015.
18. Hattori, K.; Kajimura, M.; Hishiki, T.; Nakanishi, T.; Kubo, A.; Nagahata, Y.; Ohmura, M.; Yachie-Kinoshita, A.; Matsuura, T.; Morikawa, T.; *et al.* Paradoxical ATP Elevation in Ischemic Penumbra Revealed by Quantitative Imaging Mass Spectrometry. *Antioxid. Redox Signaling* **2010**, *13*, 1157–1167.
19. Morikawa, T.; Kajimura, M.; Nakamura, T.; Hishiki, T.; Nakanishi, T.; Yukutake, Y.; Nagahata, Y.; Ishikawa, M.; Hattori, K.; Takenouchi, T.; *et al.* Hypoxic Regulation of the Cerebral Microcirculation Is Mediated by a Carbon Monoxide-Sensitive Hydrogen Sulfide Pathway. *Proc. Natl. Acad. Sci. U.S.A.* **2012**, *109*, 1293–1298.
20. Stoeckli, M.; Chaurand, P.; Hallahan, D. E.; Caprioli, R. M. Imaging Mass Spectrometry: A New Technology for the Analysis of Protein Expression in Mammalian Tissues. *Nat. Med.* **2001**, *7*, 493–496.
21. Brindle, K. M.; Bohndiek, S. E.; Gallagher, F. A.; Kettunen, M. I. Tumor Imaging Using Hyperpolarized ^{13}C Magnetic Resonance Spectroscopy. *Magn. Reson. Med.* **2011**, *66*, 505–519.
22. Webb, A. Increasing the Sensitivity of Magnetic Resonance Spectroscopy and Imaging. *Anal. Chem.* **2012**, *84*, 9–16.
23. Venables, J. A.; Spiller, G. D. T.; Hanbucken, M. Nucleation and Growth of Thin Films. *Rep. Prog. Phys.* **1984**, *47*, 399–459.
24. Venebles, J. A.; Spiller, G. D. T.; Fathers, D. J.; Harland, C. J.; Hanbucken, M. UHV-SEM Studies of Surface Processes: Recent Progress. *Ultramicroscopy* **1983**, *11*, 149–156.
25. Greeneltch, N. G.; Blaber, M. G.; Henry, A. I.; Schatz, G. C.; Van Duyne, R. P. Immobilized Nanorod Assemblies: Fabrication and Understanding of Large Area Surface-Enhanced Raman Spectroscopy Substrates. *Anal. Chem.* **2013**, *85*, 2297–2303.
26. Driskell, J. D.; Shanmukh, S.; Liu, Y.; Chaney, S. B.; Tang, X.-J.; Zhao, Y.-P.; Dluhy, R. A. The Use of Aligned Silver Nanorod Arrays Prepared by Oblique Angle Deposition As Surface Enhanced Raman Scattering Substrates. *J. Phys. Chem. C* **2008**, *112*, 895–901.
27. Suzuki, M.; Nakajima, K.; Kimura, K.; Fukuoka, T.; Mori, Y. Au Nanorod Arrays Tailored for Surface-Enhanced Raman Spectroscopy. *Anal. Sci.* **2007**, *23*, 829–833.
28. Perney, N. M. B.; Baumberg, J. J.; Zoorob, M. E.; Charlton, M. D. B.; Mahnkopf, S.; Netti, C. M. Tuning Localized Plasmons in Nanostructured Substrates for Surface-Enhanced Raman Scattering. *Opt. Express* **2006**, *14*, 847–857.
29. Helmchen, F.; Denk, W. Deep Tissue Two-Photon Microscopy. *Nat. Methods* **2005**, *2*, 932–940.
30. Le Ru, E. C.; Etchegoin, P. G. Rigorous Justification of the $|E|^4$ Enhancement Factor in Surface Enhanced Raman Spectroscopy. *Chem. Phys. Lett.* **2006**, *423*, 63–66.
31. Le Ru, E. C.; Etchegoin, P. G. *Principles of Surface-Enhanced Raman Spectroscopy and Related Plasmonic Effects*; Elsevier: Amsterdam, 2009.
32. Moskovits, M. Surface-Enhanced Raman Spectroscopy: A Brief Perspective. In *Surface-Enhanced Raman Spectroscopy: Physics and Applications*; Kneipp, K., Kneipp, H., Moskovits, M., Eds.; Springer: Heidelberg, 1989; pp 1−17.
33. Hildebrandt, P.; Stockburger, M. Surface-Enhanced Resonance Raman Spectroscopy of Rhodamine 6G Adsorbed on Colloidal Silver. *J. Phys. Chem. B* **1984**, *88*, 5935–5944.
34. Li, Y. T.; Qu, L. L.; Li, D. W.; Song, Q. X.; Fathi, F.; Long, Y. T. Rapid and Sensitive *in Situ* Detection of Polar Antibiotics in Water Using a Disposable Ag-Graphene Sensor Based on Electrophoretic Preconcentration and Surface-Enhanced Raman Spectroscopy. *Biosens. Bioelectron.* **2013**, *43*, 94–100.
35. Lin, X. M.; Cui, Y.; Xu, Y. H.; Ren, B.; Tian, Z. Q. Surface-Enhanced Raman Spectroscopy: Substrate-Related Issues. *Anal. Bioanal. Chem.* **2009**, *394*, 1729–1745.
36. Qu, L. L.; Li, D. W.; Xue, J. Q.; Zhai, W. L.; Fossey, J. S.; Long, Y. T. Batch Fabrication of Disposable Screen Printed SERS Arrays. *Lab Chip* **2012**, *12*, 876–881.
37. Toyama, A.; Hanada, N.; Abe, Y.; Takeuchi, H.; Harada, I. Assignment of Adenine Ring in-Plane Vibrations in Adenosine on the Basis of ^{15}N and ^{13}C Isotopic Frequency Shifts and UV Resonance Raman Enhancement. *J. Raman Spectrosc.* **1994**, *25*, 623–630.
38. Joshi, C. N.; Jain, S. K.; Murthy, P. S. An Optimized Triphenyltetrazolium Chloride Method for Identification of Cerebral Infarcts. *Brain Res. Protoc.* **2004**, *13*, 11–17.
39. Le Ru, E. C.; Blackie, E.; Meyer, M.; Etchegoin, P. G. Surface Enhanced Raman Scattering Enhancement Factors: A Comprehensive Study. *J. Phys. Chem. C* **2007**, *111*, 13794–13803.
40. Müller, C. B.; Loman, A.; Pacheco, V.; Koberling, F.; Willbold, D.; Richtering, W.; Enderlein, J. Precise Measurement of Diffusion by Multi-Color Dual-Focus Fluorescence Correlation Spectroscopy. *Europhys. Lett.* **2008**, *83*, 46001–p1−46001-p5.
41. Palik, E. D. *Handbook of Optical Constants of Solids II*; Academic Press: Boston, MA, 1998.
42. Lust, W. D., Ricci, A. J., Selman, W. R., Ratcheson, R. A. Methods of Fixation of Nervous Tissue for Use in the Study of Cerebral Energy Metabolism. In *Carbohydrates and Energy Metabolism*; Boulton, A. A., Baker, G. B., Butterworth, R. F., Eds.; Human Press: Clifton, NJ, 1989; pp 1−42.
43. Shintani, T.; Iwabuchi, T.; Soga, T.; Kato, Y.; Yamamoto, T.; Takano, N.; Hishiki, T.; Ueno, Y.; Ikeda, S.; Sakuragawa, T.; *et al.* Cystathionine β-synthase As a Carbon Monoxide-Sensitive Regulator of Bile Excretion. *Hepatology* **2009**, *49*, 141–150.
44. Toue, S.; Sugiura, Y.; Kubo, A.; Ohmura, M.; Karakawa, S.; Mizukoshi, T.; Yoneda, J.; Miyano, H.; Noguchi, Y.; Kobayashi, T.; *et al.* Microscopic Imaging Mass Spectrometry Assisted by on-tissue Chemical Derivatization for Visualizing

Multiple Amino Acids in Human Colon Cancer Xenografts. *Proteomics* **2013**, *14*, 810–819.

45. Kubo, A.; Ohmura, M.; Wakui, M.; Harada, T.; Kajihara, S.; Ogawa, K.; Suemizu, H.; Nakamura, M.; Setou, M.; Suematsu, M. Semi-Quantitative Analyses of Metabolic Systems of Human Colon Cancer Metastatic Xenografts in Livers of Superimmunodeficient NOG Mice. *Anal. Bioanal. Chem.* **2011**, *400*, 1895–1904.
46. Yamamoto, T.; Takano, N.; Ishiwata, K.; Ohmura, M.; Nagahata, Y.; Matsuura, T.; Kamata, A.; Sakamoto, K.; Nakanishi, T.; Kubo, A.; *et al.* Reduced Methylation of PFKFB3 in Cancer Cells Shunts Glucose Towards the Pentose Phosphate Pathway. *Nat. Commun.* **2014**, *5*, No. 3480.